



A novel data-driven auto compensation algorithm for pulsed eddy current inspection of high voltage feeder cable pipe

Xuhui Huang, Petter Wehlin, Vijay Srinivasan, Josephine Aromando & Yiming Deng

To cite this article: Xuhui Huang, Petter Wehlin, Vijay Srinivasan, Josephine Aromando & Yiming Deng (10 Mar 2025): A novel data-driven auto compensation algorithm for pulsed eddy current inspection of high voltage feeder cable pipe, Nondestructive Testing and Evaluation, DOI: [10.1080/10589759.2025.2474097](https://doi.org/10.1080/10589759.2025.2474097)

To link to this article: <https://doi.org/10.1080/10589759.2025.2474097>



© 2025 The Author(s). Published by Informa UK Limited, trading as Taylor & Francis Group.



Published online: 10 Mar 2025.



Submit your article to this journal [↗](#)



Article views: 28



View related articles [↗](#)



View Crossmark data [↗](#)

A novel data-driven auto compensation algorithm for pulsed eddy current inspection of high voltage feeder cable pipe

Xuhui Huang^a, Petter Wehlin^b, Vijay Srinivasan^c, Josephine Aromando^c
and Yiming Deng ^a

^aDepartment of Electrical and Computer Engineering, Michigan State University, East Lansing, MI, USA;

^bARIX Technologies, Houston, TX, USA; ^cConsolidated Edison of New York, Inc, New York, NY, USA

ABSTRACT

In this study, we introduce a novel auto-compensation method designed to enhance the accuracy of pulsed eddy current (PEC) measurements, crucial for non-destructive testing (NDT) in assessing the integrity of high-voltage feeder pipes. We explicitly target the unique challenges posed by strong electromagnetic interference (EMI) from internal power lines carrying three-phase alternating current. To address them, we propose a compensation algorithm that accounts for spatially varying magnetic permeability in the piping materials. The proposed method integrates multi-physics simulations of the interactions between the power lines, the pipe, and the PEC probe. Two finite element method (FEM) simulation models are developed: the Cable-Pipe Model, simulating the magnetic flux density distribution around the pipe due to internal power lines, and the PEC-Pipe Model, simulating the PEC sensing response considering the circumferentially varying magnetic permeability. To bridge the gap between computational accuracy and field deployment requirements, novel surrogate models are developed based on parametric FEM simulation datasets, allowing rapid approximation of characteristic decay time constants and nominal wall thickness estimations. Field tests validated our method's effectiveness, demonstrating a measurable reduction in false-positive indications after the physics-based compensation. This work challenges the conventional assumption of constant magnetic permeability in PEC inspections and extends the applicability of PEC for flaw detection in high-voltage feeder pipes and other challenging inspection scenarios, contributing to improved safety and infrastructure longevity.¹

ARTICLE HISTORY

Received 18 December 2024
Accepted 25 February 2025

KEYWORDS

Pulsed eddy current (PEC); non-destructive testing (NDT); high-voltage feeder cable pipe; finite element method (FEM); surrogate modeling

1. Introduction

Pulsed Eddy Current (PEC) inspection is a powerful non-destructive testing (NDT) method for evaluating the structural integrity of metallic pipelines, including those insulated or coated [1,2]. PEC leverages transient electromagnetic fields to induce eddy currents in conductive materials, enabling non-contact and potentially high-speed assessments of corrosion, wall thinning, and other subsurface defects – even when

CONTACT Yiming Deng  dengyimi@egr.msu.edu

© 2025 The Author(s). Published by Informa UK Limited, trading as Taylor & Francis Group.

This is an Open Access article distributed under the terms of the Creative Commons Attribution-NonCommercial-NoDerivatives License (<http://creativecommons.org/licenses/by-nc-nd/4.0/>), which permits non-commercial re-use, distribution, and reproduction in any medium, provided the original work is properly cited, and is not altered, transformed, or built upon in any way. The terms on which this article has been published allow the posting of the Accepted Manuscript in a repository by the author(s) or with their consent.

pipes are covered by thick insulation or protective layers [3]. By capturing the time-domain decay of these eddy currents, inspectors can estimate remaining wall thickness, detect localised damage, and gain insights into materials' electromagnetic properties. This approach is particularly beneficial for large-scale pipeline networks, as it minimises the need for insulation removal, lowers the risk of exposing hazardous coatings such as asbestos, and ultimately reduces both inspection time and costs [4]. Recent PEC research has introduced innovations in probe design – including differential probes, U-shaped probes, and focused magnetic field methods – that bolster sensitivity and resolution for pipeline defect detection [5–7]. For instance, an encircling coil configuration can scan cylindrical pipes in a single pass, while specialised magnetic field focusing techniques enhance signal-to-noise ratios in challenging environments like well casings or thick-walled offshore lines [3]. Furthermore, advanced signal processing algorithms now exploit PEC's broad frequency content, allowing robust flaw characterisation and noise suppression [8]. Efforts to integrate Giant Magnetoresistance (GMR) sensors have further boosted the detection capabilities, particularly when quantifying small defects in ferromagnetic structures [9]. Beyond these technical refinements, a growing body of work demonstrates the synergy between PEC and robotic platforms for automated, large-scale pipeline inspections. Subsea PEC systems mounted on Remotely Operated Vehicles (ROVs) can collect corrosion profiles of offshore pipelines without risking diver safety, conducting thorough scans along extended pipe sections at significant depths [6]. In-pipe robots provide similarly efficient coverage, allowing dense thickness measurements from within the pipeline – even around bends or in partially obstructed segments [4]. More recently, unmanned aerial vehicles (UAVs) equipped with PEC sensors have shown promise for remotely inspecting aboveground pipelines or elevated structures, although precise sensor alignment and lift-off control remain active research topics [5]. Collectively, these robotic integrations underscore how PEC's non-contact operation and tolerant standoff distance are ideally suited to mobile platforms, accelerating data collection and enhancing worker safety in otherwise hazardous or unreachable environments.

Electromagnetic interference (EMI), whether from industrial operations, wireless communications, or magnetic equipment, presents a significant challenge to accurate PEC-based inspections by distorting measurement signals [10]. In the context of PEC for corrosion or thickness evaluation, high-current pulsed coils and external magnets used to bias the inspection field often contribute additional noise. Researchers have tackled these EMI issues through a wide range of compensation and modelling strategies. For instance, magnetic field calibration systems have been proposed to achieve low measurement uncertainty even in noisy conditions [11], while adaptive interference suppression algorithms, such as adaptive filters, have demonstrated significant reduction in ambient magnetic noise [12]. Likewise, advanced electromagnetic field modelling techniques help predict and remove interference before and after active compensation, providing a theoretical foundation to refine system-level designs [13–15]. These modelling approaches account for unwanted coupling paths and allow accurate simulation of how external fields interact with PEC sensors. Although many interference mitigation methods focus on magnetic sensor calibration or component compensation [14], researchers have increasingly explored optimisation-based and machine learning approaches to tackle

EMI in broader engineering domains, which can also be adapted to PEC. For example, genetic algorithms can optimise discrete EMI filter components – accounting for stray parasitic elements and source impedances – to ensure electromagnetic compatibility while minimising insertion losses [16]. In healthcare monitoring contexts, analytical EMI modelling has guided the development of shielding and compensation schemes for cardiac implants subjected to external RF fields [17]. More recently, an adaptive Bayesian algorithm demonstrated robust real-time EMI mitigation in dynamic electromagnetic environments by adjusting classification boundaries as interference conditions evolve, delivering high accuracy under severe symbol error rates [18]. These approaches, combined with traditional magnetic compensation methods, have substantially increased PEC's resilience in high-interference industrial settings, particularly in the oil and gas sector, where detecting corrosion under insulation remains critical for asset integrity [19]. Overall, by integrating calibration systems, adaptive algorithms, genetic optimisation, and Bayesian decision-making, researchers continue to enhance PEC's reliability and efficiency, ensuring precise flaw detection under challenging EMI conditions.

Inspecting high-voltage feeder pipes using PEC presents unique challenges, primarily due to the strong magnetic fields generated by the power lines inside the pipe. Conventional PEC techniques assume that magnetic permeability remains constant, allowing a direct correlation between the PEC signal transient decay rate and nominal wall thickness [20]. However, the strong time-varying magnetic fields produced by the power lines inside the pipe significantly alter this assumption, particularly in proximity to the power lines, resulting in spatially varying permeability. This affects the response signal in several ways. The alternating current in the conductors produces a skin effect, concentrating the current near the inner surface of the pipe. This effect varies with frequency and can lead to non-uniform magnetic flux distributions within the pipe wall. High currents can also cause localised magnetic saturation in the ferromagnetic material, altering its permeability and consequently affecting the PEC signal. In the initial field test setup, the coating was later scraped off in an entire ring around the pipe, and Ultrasonic Testing (UT) thickness readings were taken around the complete circumference of the pipe. These readings confirmed that the pipe thickness is consistent around the circumference and that the variations seen in the PEC data are not due to actual changes in the pipe wall thickness. Properly removing the coating to get accurate UT thickness readings was crucial for validating the PEC measurements. This further confirmed that the assumption of homogeneous magnetic permeability along the pipe's circumferential dimensions is invalid. Such inconsistencies can cause false positive flaw detections, resulting in unnecessary maintenance or undetected critical failures.

To address these limitations, a novel compensation methodology is proposed in this paper that accounts for spatially varying permeabilities and effectively mitigates electromagnetic interference from time-varying magnetic fields generated by power lines inside the pipe. This approach integrates multi-physics simulations of the interactions between the power lines, the pipe, and the PEC probe. It integrates two FEM models: the Cable-Pipe Model, which accurately simulates the electromagnetic field distribution, and the PEC-Pipe Model, which simulate the PEC transient response under varying conditions. The Cable-Pipe Model simulates the magnetic flux density distribution around the ferromagnetic pipe wall due to the power lines inside the pipe, incorporating precise

geometrical parameters and the material's nonlinear B - H characteristics to yield the corresponding relative magnetic permeability.

To further enable in situ inspections over designated scan zones and minimise computational complexity, surrogate models are developed trained on parametric FEM simulation datasets. These surrogate models' approximate FEM simulation results based on input pipe dimensions, facilitating rapid predictions of the decay time constants and wall thickness without the need for costly numerical computations. The compensation methodology incorporates a calibration protocol, the generation of a simulated dataset for accurate transient decay time prediction under various conditions, and inhomogeneous permeability distribution. By correlating experimental and simulation through a scaling coefficient, the proposed method significantly enhances the reliability and computational efficiency of PEC measurements in challenging electromagnetic interference environments, improving its robustness for flaw detection in high-voltage feeder pipes.

By integrating calibration, simulation-based predictive modelling, and surrogate-based fast compensation, this methodology represents a significant advancement in non-destructive evaluation (NDE), offering a scalable and adaptable solution to a prevalent inspection challenge. The integration of two simulations, despite their inherent simplifications, achieves a practical compromise between accuracy and field applicability. Enhancing the reliability of PEC inspections in complex electromagnetic environments where standard assumptions about electromagnetic material properties are invalid can improve operational safety, inspection efficiency, and cost-effectiveness in evaluating high-voltage feeder pipes and other critical infrastructure components.

2. Analytical model for compensation algorithms

In the inspection of high-voltage feeder pipes using PEC, internal power lines inside the pipe introduce significant challenges due to the time-varying magnetic fields they generate. They affect the local relative magnetic permeability $\mu_r(\theta)$ of the ferromagnetic carbon steel, leading to inaccuracies in wall thickness assessments if not properly accounted for. Consider a cylindrical pipe with an inner radius R containing an internal cable carrying a current I , and located at an angular position $\theta_c = 180^\circ$ as shown in [Figure 1](#). Cable placement follows an eccentric configuration with a normalised offset $L = R/2$ from the longitudinal axis. While the input carries some uncertainties, the model still captures key EMI pattern characteristics. This will determine the magnetic field intensity $H(\theta)$ at various locations along the circumferential direction, which is critical for understanding the variation in relative magnetic permeability $\mu_r(\theta)$ and its subsequent effect on PEC measurements.

The distance $r(\theta)$ from the centre of the cable to a point on the inner surface of the pipe at angular position θ is calculated using:

$$r(\theta) = \sqrt{R^2 + L^2 - 2RL \cos(\theta - \theta_c)}. \quad (1)$$

Applying Ampère's Law for a long, straight conductor, the magnetic field intensity $H(\theta)$ at a distance $r(\theta)$ from the conductor is given by:

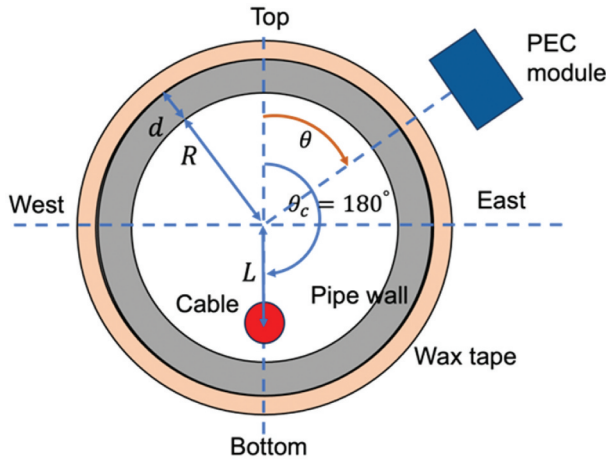


Figure 1. Cross-section view of the pipe with internal cable.

$$H(\theta) = \frac{I}{2\pi r(\theta)} \quad (2)$$

For this geometry, the maximum field intensity occurs at $\theta = \theta_c$. Ferromagnetic materials, such as carbon steel, exhibit a nonlinear relationship between the magnetic flux density B and the magnetic field intensity H , known as the magnetisation curve or B-H curve. As H increases, the material approaches magnetic saturation, and the relative magnetic permeability μ_r decreases, asymptotically approaching the magnetic permeability of free space μ_0 . This relationship can be characterised using material-specific magnetisation curves illustrated in Figure 2.

Specifically, the relative magnetic permeability can be expressed as:

$$\mu_r(\theta) = \frac{f_{BH}(H(\theta))}{\mu_0 H(\theta)} \quad (3)$$

As the magnetic field intensity $H(\theta)$ varies around the circumference due to the offset cable, $\mu_r(\theta)$ becomes position-dependent. Existing studies have investigated the

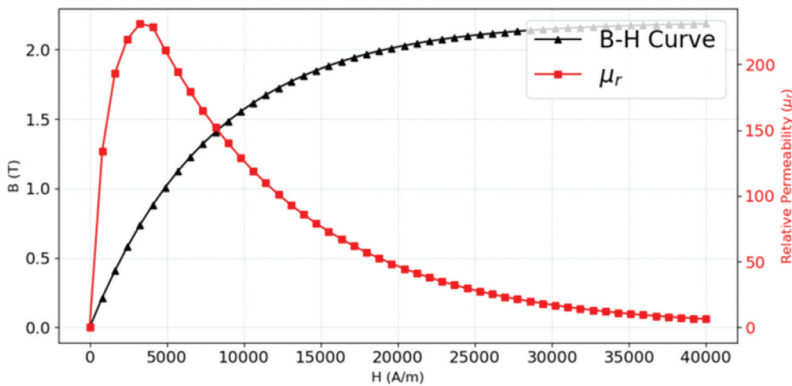


Figure 2. Relative permeability versus magnetic field intensity.

dominant time constant c_1 , which is related to the material properties under investigation, specifically magnetic permeability μ , electrical conductivity σ , and wall thickness d . Previous work has shown that the dominant time constant behaves as $c_1 \propto \frac{1}{\mu_r \sigma d^2}$, which directly leads to $\tau \propto \mu_r \sigma d^2$ [21,22], where τ is the characteristic decay time. Since this relationship has been validated for flat plates and can be extended to curved surfaces, such as large-diameter pipes, considering a pipe with cable position-dependent permeability $\mu_r(\theta)$, results in a dominant time constant that varies along the circumferential direction. Thus, the dominant time constant becomes:

$$\tau(\theta) \propto \mu_r(\theta) \sigma d^2 \quad (4)$$

If we assume a constant permeability $\hat{\mu}_r$ during the calibration or modelling process but in reality, the permeability is position-dependent, the estimated time constant $\hat{\tau}$ will differ from the actual time constant $\tau(\theta)$. Assuming that the wall thickness d remains constant in both calculations, the predicted wall thickness can be derived from the ratio between the assumed permeability and the actual permeability:

$$d_{\text{predicted}} = d_{\text{actual}} \sqrt{\frac{\mu_r(\theta)}{\hat{\mu}_r}}$$

In field inspections, the lift-off distance l , defined as the separation between the PEC probe and the pipe surface, is subject to significant variability. These pipes, constructed from carbon steel, are often coated with wax tape as shown in Figure 3(a). The presence of various coatings, surface roughness, and probe positioning errors contribute to variations in l . Additionally, the pipes are installed in both horizontal and vertical orientations, with certain sections featuring wrapped wax tape insulation. Waxes are generally poor conductors of electricity, and wax tape, in particular, exhibits a relative permeability μ_r close to that of free space μ_0 , effectively rendering them electrically and magnetically similar to air [23]. To facilitate high-resolution PEC data collection along these feeder cable pipes, a robotic platform was developed and deployed. This system is engineered to navigate the exterior surface of the pipes vertically and horizontally, equipped with PEC probe and associated data acquisition hardware. In the existing studies, l is utilised as a critical parameter in PEC signal interpretation. However, the

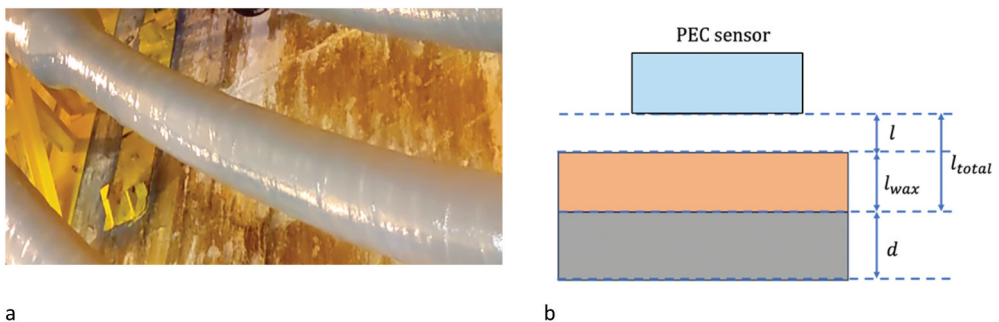


Figure 3. (a) Field test with wax tape insulation covering the pipe surface (b) Schematic diagram of PEC sensor positioned above the pipe surface with wax tape.

substantial wax tape thickness variation introduces considerable variance in l_{wax} , as shown in Figure 3(b), thereby affecting the PEC signal. Given the analysis of wax tape properties, it is justifiable to model it as an air-like medium within the mathematical framework. Under this approximation, the effective lift-off can be redefined as the sum of the traditional lift-off distance and the thickness of the wax tape insulation. Mathematically, this equivalent lift-off is expressed as:

$$l_{total} = l + l_{wax}$$

By incorporating l_{wax} into the mathematical model, we effectively account for the variations introduced by the wax tape. We incorporate lift-off into our mathematical model similar to the model proposed in [24,25]. The induced voltage $V(t, l)$ in the receiver coil, considering lift-off, can be expressed as:

$$V(t, l) = b_1 e^{-\frac{\pi^2 t}{\mu_r(\theta) \sigma d^2} e^{-kl}} + \sum_{i=2}^{\infty} b_i e^{-c_i t}$$

where b_1 and b_i are coefficients dependent on the system parameters related to the sensor configuration, c_i are higher-order time constants, and k is a constant that accounts for the exponential attenuation due to lift-off. When truncating the response signal after the excitation decreases to zero, the higher-order terms become negligible, and the expression simplifies to:

$$V(t, l) = b_1 e^{-\frac{\pi^2 t}{\mu_r(\theta) \sigma d^2} e^{-kl}}$$

Taking the logarithm of both sides and differentiating with respect to time:

$$\frac{d}{dt} \ln[V(t, l)] = -\frac{\pi^2}{\mu_r(\theta) \sigma d^2}$$

Notably, the time derivative $\frac{d}{dt} \ln[V(t, l)]$ is independent of l , which indicates that the decay rate is unaffected by lift-off variations, allowing for reliable wall thickness estimation even when lift-off varies. Therefore, the estimated thickness can be expressed as:

$$d = \sqrt{\frac{\pi^2}{\mu_r(\theta) \sigma} \left(-\frac{d}{dt} \ln[V(t, l)] \right)^{-1}}$$

The state-of-the-art method adopts the estimated time derivative based on the assumed constant $\widehat{\mu}_r$, therefore causing the prediction error:

$$Predictionerror(\theta) = \left| \frac{\pi}{\sqrt{\sigma \left(\frac{d}{dt} \ln[V(t, l)] \right)}} \left(\sqrt{\frac{1}{\widehat{\mu}_r}} - \sqrt{\frac{1}{\mu_r(\theta)}} \right) \right|$$

To account for the variability in $\mu_r(\theta)$, we introduce a compensation factor $C(\theta)$ defined as:

$$C(\theta) = \sqrt{\frac{\widehat{\mu}_r}{\mu_r(\theta)}}$$

By applying $C(\theta)$, we reduce the impact of permeability variability on thickness estimation and improve the accuracy of the PEC measurement for detecting pipe wall thinning. However, while $C(\theta)$ is effective under the assumption of constant wall thickness, it becomes inadequate when wall thinning occurs. This is because the wall thickness d becomes a function of the angular position θ , i.e. $d = d(\theta)$, leading to an interdependency between $\mu_r(\theta)$ and $d(\theta)$. In this context, the relative permeability becomes dependent on both θ and $d(\theta)$:

$$\mu_r(\theta, d(\theta)) = \frac{f_{BH}(H(\theta, d(\theta)))}{\mu_0 H(\theta, d(\theta))}$$

where f_{BH} represents the B-H curve function. Determining $\mu_r(\theta, d(\theta))$ analytically is complex due to its dependence on the pipe geometry and wall thickness variations. This complexity demands a different approach. In this paper, we compute the average permeability over discrete angular segments to account for the spatial variations in both μ_r and d . To achieve this, we discretise the pipe into N angular regions matching the number of scan lines (e.g. 8 or 16 lines). For each discrete region i , we compute the mean relative permeability $\mu_{r,i}$ as:

$$\mu_{r,i} = \frac{1}{\Delta\theta_i} \int_{\theta_i}^{\theta_i+\Delta\theta_i} \mu_r(\theta, d(\theta)) d\theta$$

This discretisation allows us to approximate each angular sector with a representative permeability value $\mu_{r,i}$, capturing the coupled effects of μ_r and d variations. The theoretical numerical model is shown in Figure 4(a).

The complexity of modelling three-phase AC fields, ferromagnetic pipe, and PEC probe dynamics in a single FEM simulation becomes very time-consuming when accounting for both microsecond pulses and millisecond eddy current decay, despite

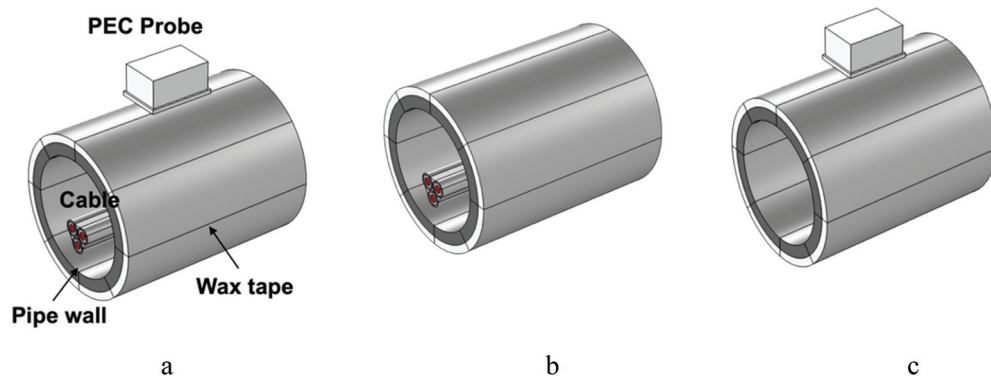


Figure 4. (a) Fully coupled FEM model (b) *Cable-pipe Model*: frequency-domain analysis of magnetic fields from internal cables (c) *PEC-pipe Model*: time-domain simulation of transient eddy current decay.

its theoretical feasibility. The complexity stems from solving both rapid field changes and interactions using fine mesh elements, while simultaneously modelling the complete cable bundle, pipe structure, and probe geometry. Moreover, using pre-defined B-H curves for ferromagnetic pipe materials requires iterative calculations at each time step, creating substantial computational overhead when analysing PEC responses across hundreds of milliseconds-scale intervals. At each time step, the solver recalculates local permeabilities, solves the system, and then proceeds to the next step, causing an exponential increase in run time. To address this issue, we divide the system into two FEM models, as shown in Figure 4(b). The initial framework employs a frequency-domain Cable-Pipe Model to characterise both the 60 hz current-generated magnetic fields and their induced non-uniform pipe magnetisation effects. In the example of Figure 4(a), the internal power lines consist of three cables arranged in a triangular formation, each with a lead diameter of 15 mm. A refined mesh is used, particularly around the cables and the inner pipe wall. This setup yields a varying distribution around the pipe circumference. Second, a time-domain PEC – Pipe Model – depicted in Figure 4(c)—is dedicated to the transient response of the pulsed eddy current probe. As illustrated in Figure 5(a), it incorporates the calculated spatial permeability variations to simulate the PEC response, assigning the appropriate values to each circumferential segment of the pipe wall. By doing so, both permeability variations and wall-thickness loss are accurately captured. However, performing FEM simulations for every pipe profile can still be computationally expensive, underscoring the benefits of this two-model approach.

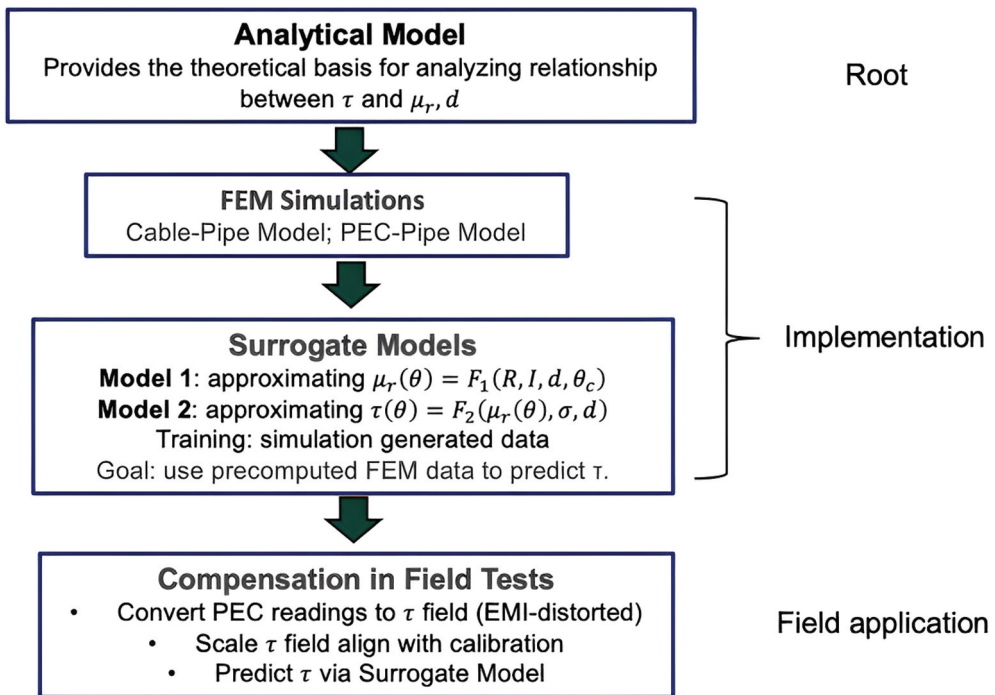


Figure 5. Workflow for field test compensation.

3. Surrogate models

To address the computational complexities associated with FEM simulations for varying pipe parameters – especially crucial for real-time applications in field inspections – we have developed surrogate models that approximate FEM simulation results based on input parameters as shown in Table 1. They are constructed using Gaussian Process Regression (GPR) with a sparse formulation and an RBF (Radial Basis Function) kernel, enabling efficient modelling of complex, nonlinear relationships with quantified uncertainties. By embedding the direct computation of τ into the surrogate model, we can rapidly predict decay time constants $\tau(\theta)$ for different $\mu_r(\theta)$ and $d(\theta)$ without running extensive FEM simulations during inspections. This allows for rapid predictions of decay time constants and wall thickness without extensive computations, thereby enhancing the efficiency and effectiveness of PEC measurements in detecting pipe wall thinning. Moreover, τ alignment is incorporated into the surrogate model to remove the scaling factor regarding simulation predictions and field measurements. This alignment ensures that the predictions are accurate and reliable. By precomputing and storing FEM simulation data for different pipe profiles, these surrogate models enable rapid retrieval of results, significantly reducing computation time during real-time inspections.

The surrogate modelling framework implements a two-stage approach to replace computationally expensive FEM simulations. The first surrogate model maps pipe parameters to the spatial distribution of relative permeability approximating the function of $\mu_r(\theta) = F_1(R, I, d, \theta_c)$. The second stage, the PEC-Pipe surrogate, transforms this permeability distribution along with other parameters into characteristic decay times $\tau(\theta) = F_2(\mu_r(\theta), \sigma, d)$.

We illustrate the overall workflow from analytical foundations to rapid field application. After establishing the theoretical relationships in the Analytical Model, two FEM simulations generate parametric datasets. These datasets train two corresponding models: Model 1 approximates $\mu_r(\theta)$ given pipe and cable parameters from simulation of Cable-Pipe, while Model 2 predicts $\tau(\theta)$ using the inferred $\mu_r(\theta)$ from simulation of PEC-Pipe. Finally, the surrogate predictions are used in Compensation during field tests to correct for EMI-distorted signals and obtain accurate pipe wall thickness assessments in real time. Overall, we underscore the practical deployment of surrogate-based compensation, bridging analytical model with field-ready, computationally efficient methods. At the core of the surrogate modelling is the need to predict two primary outputs: the relative magnetic permeability distribution $\mu_r(\theta)$ around the pipe's circumference due to the internal cable's magnetic field, and the corresponding decay time constants $\tau(\theta)$ from the PEC measurements. To build our surrogate models, we generated a parametric

Table 1. Inputs and outputs of surrogate models.

Surrogate Models for Approximation	Input	Output
Cable–Pipe Model F_1	Cable current I pipe dimensions R wall thickness d angular position θ_c of cable	Relative permeability $\mu_r(\theta)$
PEC–Pipe Model F_2	Relative permeability $\mu_r(\theta)$ electrical conductivity σ wall thickness d .	Characteristic decay time constant $\tau(\theta)$

dataset by varying the pipe radius (R) and wall thickness (d). Specifically, we sampled R from 75 mm to 175 mm in increments of 5 mm, resulting in 21 unique outer diameters. For each R , we set the d from 5 mm to 15 mm in 1 mm steps, yielding 11 distinct thickness values. We conducted dual FEM simulations for each of 231 geometric configurations to extract both permeability distributions and temporal decay characteristics. The resulting dataset serves as training input, ensuring coverage across a broad range of realistic pipe sizes and thicknesses. The surrogate model relies on GPR, which models nonlinear relationships by treating outputs as Gaussian process realisations defined by mean and covariance functions, while providing uncertainty quantification. Specifically, GPR models the relationship between the inputs \mathbf{X} and outputs \mathbf{y} as:

$$\mathbf{y} = f(\mathbf{X}) + \epsilon,$$

where $f(\mathbf{X})$ is an unknown latent function sampled from a Gaussian process, and $\epsilon \sim \mathcal{N}(0, \sigma_n^2 I)$ represents independent and identically distributed Gaussian noise with variance σ_n^2 . The latent function $f(\mathbf{X})$ is characterised by a Gaussian process:

$$f(\mathbf{X}) \sim \mathcal{GP}\left(m(\mathbf{X}), k(\mathbf{X}, \mathbf{X}')\right)$$

where $m(\mathbf{X})$ is the mean function, often set to zero without loss of generality, and $k(\mathbf{X}, \mathbf{X}')$ is the covariance function or kernel that encodes the relationship between data points. For the surrogate models, the Radial Basis Function (RBF) kernel, also known as the Gaussian kernel, is chosen due to its smoothness and infinite differentiability properties, which are suitable for modelling the underlying physics of the problem. The RBF kernel is defined as:

$$k(x_i, x_j) = \sigma_f^2 \exp\left(-\frac{1}{2}(x_i - x_j)^\top \Lambda^{-1}(x_i - x_j)\right),$$

where σ_f^2 is the signal variance, controlling the vertical scale of the function variances, and $\Lambda = \text{diag}(l_1^2, l_2^2, \dots, l_p^2)$ is a diagonal matrix of squared length-scale parameters. The input vectors x_i, x_j correspond to different observations.

The RBF kernel measures the similarity between input points, with greater values indicating more closely related inputs leading to similar outputs. The surrogate models are trained using datasets generated from FEM simulations. The training process involves optimising the hyperparameters $\sigma_f^2, \Lambda, \sigma_n^2$ of the GPR model. This is typically done by maximising the log-marginal likelihood function, which balances data fit and model complexity:

$$\log p(\mathbf{y}|\mathbf{X}, \theta) = -\frac{1}{2}\mathbf{y}^\top (K + \sigma_n^2 I)^{-1} \mathbf{y} - \frac{1}{2} \log |K + \sigma_n^2 I| - \frac{n}{2} \log 2\pi,$$

where K is the kernel matrix computed using the RBF kernel for all pairs of training inputs, n is the number of training data points, and θ represents all the hyperparameters. We maintain separate models that preserve physical interpretability but require sequential execution, therefore, to achieve physical transparency and facilitate model validation. By optimising these hyperparameters and incorporating a τ -alignment step that uses calibration points where the field-measured decay times $\tau_{\text{calibration from field}, i}$ are known

and the predicted decay time constants $\tau_{\text{simulation},i}$ can be scaled with a factor of α and by minimising

$$RMSE = \sqrt{\frac{1}{N} \sum_{i=1}^N (\tau_{\text{calibration from field},i} - \alpha \tau_{\text{simulation},i})^2}$$

We initial the model with $\sigma_s^2 = 1.0$ for signal variance, length scales of 1.0 and noise variance σ_n^2 of 0.01. Then these hyperparameters are optimised using the Limited-memory Broyden-Fletcher-Goldfarb-Shanno-Bounds (L-BFGS-B), converging to $\sigma_s^2 = 0.82$. The model is further refined through τ -alignment with field measurements, enabling accurate real-time predictions. In summary, we implement two surrogates, approximating the underlying Cable-Pipe and PEC-Pipe numerical models. Firstly, we train a GPR surrogate to approximate F_1 . Next, we build a second surrogate to approximate F_2 to predict $\tau(\theta)$. Mathematically, this yields an approximate hierarchical sequential function of $\tau(\theta) = F_2(F_1(R, I, d, \theta_c), \sigma, d)$, allowing us to skip running FEM every time. Each GPR uses the RBF kernel described above and is trained by maximising the log-marginal likelihood on a parametric dataset of FEM simulations. Moreover, for comparison between FEM and GPR in terms of computational efficiency and practicality for field inspections. FEM simulations, while accurate, require 1 hour per prediction due to their mesh-dependent complexity, necessitating high-performance computing (HPC) resources. In contrast, the GPR surrogate model achieves real-time predictions (less than 2 minutes) after a one-time training phase, with fixed prediction complexity. This efficiency allows deployment on lightweight hardware (e.g. inspection robots), bypassing the need for HPC clusters. While FEM is indispensable for generating training data, the GPR surrogate bridges the gap between physical accuracy and operational feasibility, enabling scalable, real-time wall thickness monitoring in EMI-heavy environments.

4. Field tests results and discussion

In this section, we present the results of field tests conducted to validate the effectiveness of the proposed auto-compensation algorithm in real-world PEC inspections of high-voltage feeder pipes. We analyse the performance of the algorithm across multiple pipe segments, compare compensated and uncompensated measurements, and discuss the practical implications of our findings.

Figure 6 illustrates the deployment of the PEC inspection system in an underground tunnel environment, characterised by space constraints and complex arrangements of high-voltage feeder pipes. Despite these challenges, the inspection system, enhanced by our compensation algorithm, operated effectively, ensuring accurate data collection. To thoroughly assess the pipe surfaces, we employed a dual scanning strategy. First, we conduct scans at 45° intervals around the pipe's circumference to accurately capture wall thickness and account for magnetic permeability variations due to internal cables. Next, we employed an axial scanning method, during which sensors traversed the entire length of the pipe, systematically covering the axial direction to map wall thickness variations longitudinally. Calibration of the PEC instrument was critical for ensuring accuracy. We initiated the process by attaching the encoder and preparing the system for scanning. An

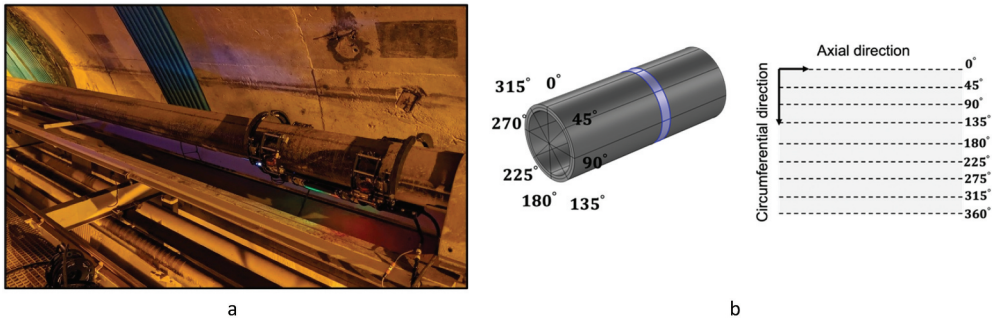


Figure 6. (a) Field deployment of PEC inspection system on high-voltage feeder pipes in an underground tunnel (b) Schematic representation of circumferential scan positions and corresponding axial scan lines.

initial point scan targeted areas with near 100% nominal wall thickness and minimal insulation, serving as a baseline. We then identified an optimal reference point with a higher signal amplitude and slower decay rate, corresponding to the nominal (100%) wall thickness. Calibrating at both the beginning and end of each inspection cycle ensured probe stability and compensated for any system drift, thereby enhancing measurement reliability.

Table 2 summarises the tested pipe segments specifications, including six horizontal and two vertical carbon steel pipes from different feeder lines. Notably, segments PS17–19 through PS30–14 from Feeder Line 34,051 had available ultrasonic testing (UT) validation data. The removal of protective coatings allowed for UT measurements, which confirmed consistent wall thickness and indicated that any detected anomalies in uncompensated PEC data were false positives due to electromagnetic interference rather than actual material loss. All pipes shared similar material properties and were inspected using the PEC-025-G2 probe under consistent configurations, although scan modes varied between dynamic and grid mapping. The uniform dimensions (outer diameters and wall thicknesses) facilitated comparative analysis. Data quality metrics showed low

Table 2. Pipe segment and inspection specifications.

Pipe ID	Type/Feeder	Dimensions (R/d/Wax Tape Coating)	Coverage	No. lines	Validation Status
PS17–19	Horizontal F34051	R: 109.5 mm; d: 6.35 mm Coating: 6.35 mm	L: 7315.2 mm Circ: 728.1 mm	8	UT Verified
PS23–25	Horizontal F34051	R: 109.5 mm d: 6.35 mm Coating: 6.35 mm	L: 7315.2 mm Circ: 728.1 mm	8	UT Verified
PS29–30	Horizontal F34051	R: 109.5 mm d: 6.35 mm Coating: 6.35 mm	L: 7315.2 mm Circ: 728.1 mm	8	UT Verified
PS30–14	Horizontal F34051	R: 109.5 mm d: 6.35 mm Coating: 6.35 mm	L: 7315.2 mm Circ: 728.1 mm	8	UT Verified
PS93–92	Horizontal F63	R: 136.5 mm d: 6.35 mm Coating: 6.35 mm	L: 7315.2 mm Circ: 897.7 mm	16	N/A
PS100–99	Horizontal F63	R: 136.5 mm d: 6.35 mm Coating: 6.35 mm	L: 7315.2 mm Circ: 897.7 mm	16	N/A
Vertical-4	Vertical	R: 136.5 mm d: 6.35 mm No Coating	L: 6096 mm Circ: 897.7 mm	4	N/A
Vertical-8	Vertical	R: 136.5 mm d: 6.35 mm No Coating	L: 6096 mm Circ: 897.7 mm	8	N/A

warning percentages (1.52% to 3.93%) for the F34051 segments. The frequent false-positive wall loss indications in uncompensated PEC data underscored the necessity of our compensation algorithm. While UT validation was possible for accessible areas, some uncertainty remains for non-validated sections due to inaccessibility. Nevertheless, the compensation algorithm demonstrated improved accuracy across all tested segments, reducing false positives and enhancing the reliability of PEC inspections.

Figure 7 presents the probability density distributions of wall thickness measurements for four segments, comparing compensated and uncompensated PEC data. The compensated measurements exhibit higher means and significantly lower standard deviations, indicating enhanced accuracy and precision. For the PS17–19 segment, the mean increased from 96.05% to 98.94%, while the standard deviation was reduced from 7.12% to 1.40%. Similarly, PS23–25 measurements saw an increase in mean from 98.68% to 99.41% with a corresponding reduction in variability. In the PS29–30 segment, the mean rose from 91.43% to 100.33%. Lastly, the PS30–14 segment showed an increase in mean from 89.71% to 100.53%. Unlike the other three segments, PS30–14 shows large post-compensation variance, likely due to the split-cable configuration, where two separate cables generate independent magnetic field variations. Such field interactions produce complex circumferential magnetic patterns that deviate from single-cable simulations. This geometric mismatch effect will be the focus of subsequent studies. These results demonstrate that the compensation algorithm effectively corrects underestimations caused by magnetic interference, aligning the measurements closely with the nominal

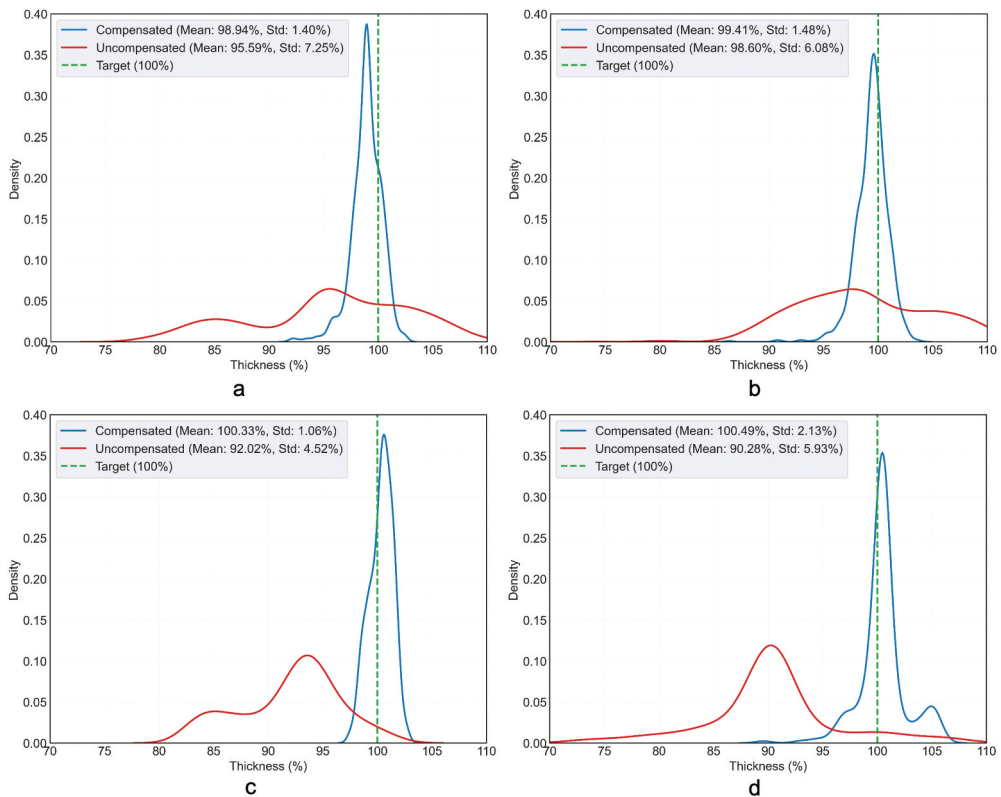


Figure 7. Probability density distributions of wall thickness measurements comparing compensated (blue) and uncompensated (red) PEC inspections for four pipe segments: (a) PS17–19 (b) PS23–25 (c) PS29–30 and (d) PS30–14.

wall thickness of 100%. The reduced standard deviations reflect improved measurement consistency. While some uncertainty persists in non-validated areas, the overall enhancement in data quality underscores the practical value of the compensation algorithm in field applications.

Figure 8 and Figure 9 provide polar visualisations of wall thickness distributions for pipe segments PS17–19 and PS30–14, respectively. Each polar plot uses a clockwise angular reference system starting from 0° (top), with 45° intervals marking eight circumferential sectors. The radial dimension represents normalised wall thickness, with concentric rings indicating percentage values from 20% to 120% relative to the nominal thickness. The colour scale ranges from yellow through light blue to dark blue providing intuitive visualisation of thickness variations. Before Compensation, both figures show significant underestimations in specific angular sectors (e.g. 270°–315° for PS17–19 and 270°–0° for PS30–14), with measurements indicating up to 20% false material loss. These discrepancies are attributed to magnetic field interference from internal power cables. The spotted false material loss reflect magnetic field interference from the internal power

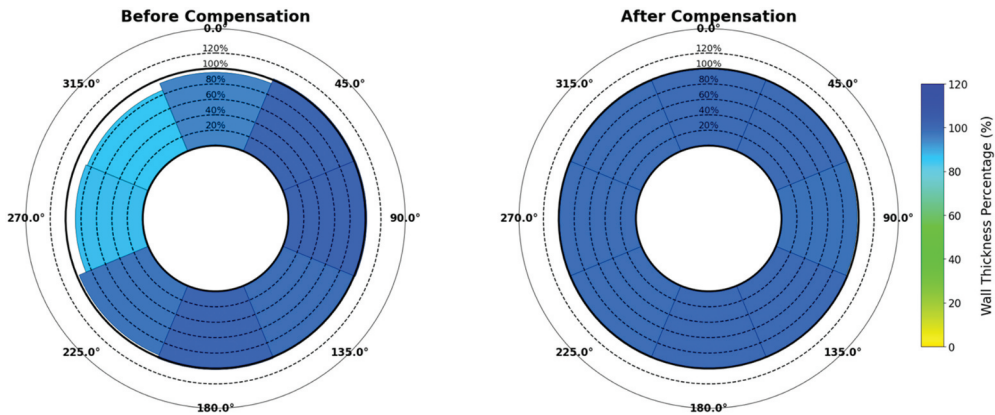


Figure 8. PS17–19 polar visualization of wall thickness distribution before and after compensation.

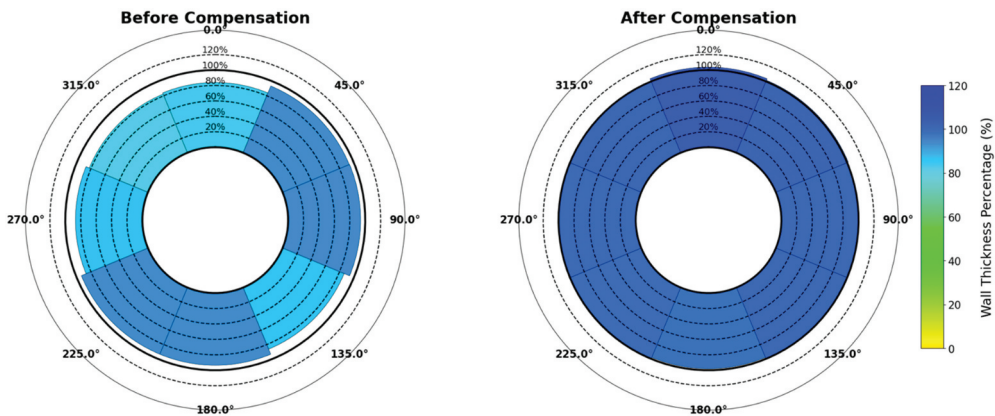


Figure 9. PS30–14: comparative polar plots of wall thickness distribution before and after compensation.

cables, especially where cable eccentricity or cable bundles produce localised EMI effects. After Compensation, the measurements uniformly range from 95% to 105% of the nominal thickness in all segments. This uniformity confirms the algorithm's effectiveness in correcting spatial measurement errors and aligns with UT validations of consistent wall thickness. The correction of the double-dip pattern in PS30–14 suggests that the algorithm successfully addresses complex interference patterns, potentially caused by the configuration of the internal three-phase power cables. These visualisations reinforce the practical applicability of the compensation algorithm in enhancing inspection accuracy.

Results of Vertical-8 is shown in [Figure 10](#) with eight 45° intervals on a polar grid. Reference circles at 0%, 70%, and 100% nominal thickness are shown, with compressed scaling below 70% to enhance visualisation. Before compensation, significant measurement variability is evident, particularly at 270° and 315°. After compensation, median values align near 100% nominal thickness with reduced interquartile ranges, indicating enhanced accuracy and consistency.

[Figure 11](#) displays radial box plots for segment PS100–99, comparing pre-and post-compensation at 16 circumferential positions (22.5° intervals) on a polar grid with reference circles at 0%, 70%, and 100% nominal thickness. For this horizontal pipe segment inspected at 16 circumferential positions, the pre-compensation data shows heterogeneous interquartile ranges and medians deviating from the nominal thickness. Post-compensation, the measurements display uniform medians near 100%, reduced variability, and consistent whisker lengths across all angles. These results affirm that the compensation algorithm effectively corrects systematic biases and reduces measurement variability regardless of pipe orientation or surface conditions. The algorithm's ability to improve accuracy in both coated horizontal pipes and uncoated vertical pipes underscores its practical applicability in diverse field environments. While the proposed method significantly improves measurement accuracy, limitations exist. The algorithm's performance in non-validated sections of the pipes remains uncertain due to the lack of UT or visual

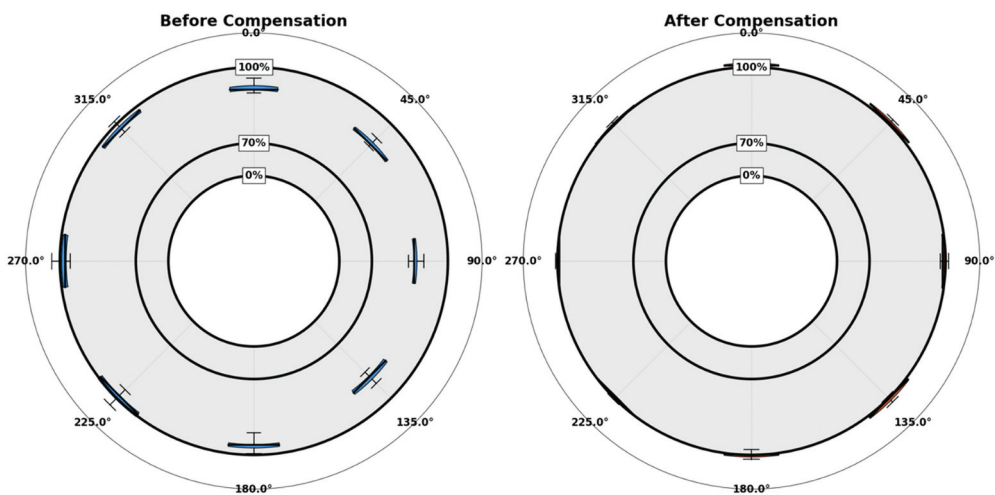


Figure 10. Vertical-8 radial box plots displaying the wall thickness distribution before and after compensation.

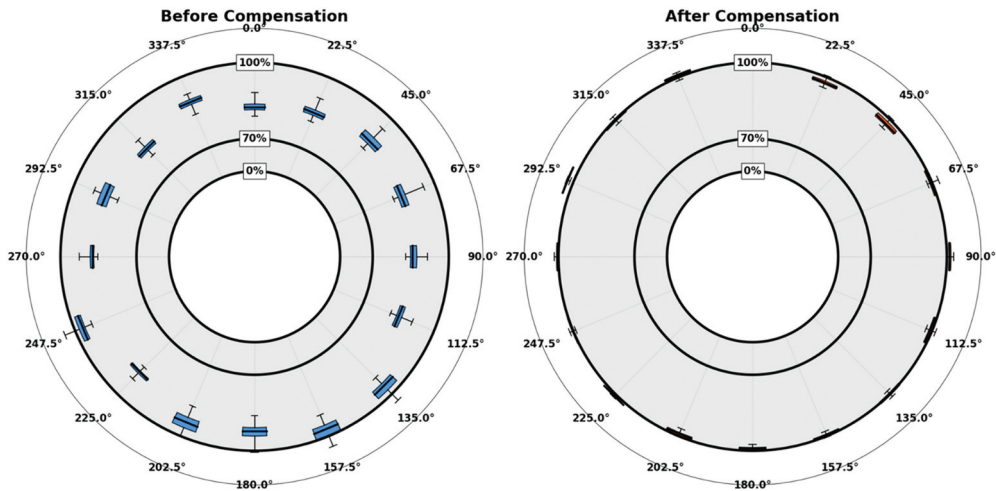


Figure 11. PS100-99 radial box plots showing wall thickness distribution before and after compensation.

inspection data. Additionally, the algorithm assumes uniform material properties, which may not account for anomalies like localised corrosion or material defects.

Future studies should focus on validating the algorithm in sections inaccessible to UT measurements, Future studies should not only focus on validating the algorithm in sections inaccessible to UT measurements but also extend testing to real-world conditions where pipes may experience natural corrosion processes, heterogeneous wall loss patterns, and other in-service degradation mechanisms. Incorporating deep learning could enhance the algorithm's ability to detect and compensate for localised anomalies, further improving the reliability of PEC inspections.

5. Conclusion and future work

This paper presents a novel approach to enhancing the accuracy of Pulsed Eddy Current (PEC) measurements for the inspection of high-voltage feeder pipes. By introducing new physics-based models that, for the first time, effectively compensate for signal distortions caused by internal magnetic fields, we have significantly improved PEC measurement accuracy. These models account for spatially varying magnetic permeability induced by internal current-carrying conductors, addressing a critical challenge that previously led to erroneous assessments of material integrity. The proposed integrated compensation methodology combines empirical data, finite element method (FEM) simulations, and Gaussian Process Regression (GPR) surrogate models. This integration enables accurate pipeline integrity assessments to be conducted within minutes, making the approach practical for in situ inspections and real-time applications. The use of surrogate models reduces computational demands without compromising accuracy, facilitating rapid and precise wall thickness estimations. The compensation methods and accompanying software tool have been

validated through field demonstrations on in-service pipelines. Deploying the system in challenging underground tunnel environments confirmed its effectiveness and robustness. For future development, we identify several promising directions. First, we plan to extend our surrogate modelling framework to handle cable split scenarios and more diverse operating conditions. This includes developing enhanced models that can account for complex electromagnetic field interactions in split-cable scenarios. Second, we aim to implement automated parameter updating capabilities to dynamically adjust compensation factors based on real-time measurements. Third, we will explore hardware-level solutions such as EMI shielding to complement our software-based compensation approach. Finally, we plan to expand our validation studies across a broader range of pipe specifications and operating conditions through increased industry collaboration. These developments will further strengthen the practical applicability of our method while potentially extending its benefits to other NDT techniques affected by variable magnetic permeability.

Note

1. A provisional patent application covering the proposed method has been filed (U.S. Patent Application No. 18/756,422).

Acknowledgments

The authors wish to thank the ARIX team members, particularly Ben Comperry, Tyler Flanagan, and Joshua Pagel, for their invaluable support during the two field testings. Their expertise contributed significantly to the successful implementation and validation of the proposed compensation methodology in real-world inspection scenarios.

Disclosure statement

No potential conflict of interest was reported by the author(s).

ORCID

Yiming Deng  <http://orcid.org/0000-0001-5958-3683>

References

- [1] Sophian A, Tian G, Fan M. Pulsed eddy current non-destructive testing and evaluation: a review. *Chin J Mech Eng*. 2017;30(3):500–514. doi: [10.1007/s10033-017-0122-4](https://doi.org/10.1007/s10033-017-0122-4)
- [2] Chen X, Liu X. Pulsed eddy current-based method for electromagnetic parameters of ferromagnetic materials. *IEEE Sensors J*. 2021;21(5):6376–6383. doi: [10.1109/JSEN.2020.3038203](https://doi.org/10.1109/JSEN.2020.3038203)
- [3] Liu C, Dang B, Wang H, et al. Synthesized magnetic field focusing for the non-destructive testing of oil and gas well casing pipes using pulsed eddy-current array. *IEEE Trans Magn*. 2022;58(9):1–10. doi: [10.1109/TMAG.2022.3186548](https://doi.org/10.1109/TMAG.2022.3186548)

- [4] Valls Miro J, Ulapane N, Shi L, et al. Robotic pipeline wall thickness evaluation for dense nondestructive testing inspection. *J Field Robot.* 2018;35(8):1293–1310. doi: [10.1002/rob.21828](https://doi.org/10.1002/rob.21828)
- [5] Yu Z, Yang F, Fu Y, et al. Investigation of focusing properties of probes for pulsed eddy current testing. *IEEE Sensors J.* 2021;21(23):26830–26838. doi: [10.1109/JSEN.2021.3121147](https://doi.org/10.1109/JSEN.2021.3121147)
- [6] Slomp E, Bertelli M, Milijanovic D. Subsea PEC: the NDT diverless robotic system for the pipeline corrosion inspection. *Abu Dhabi International Petroleum Exhibition and Conference Abu Dhabi*; 2012 doi:[10.2118/161662-MS](https://doi.org/10.2118/161662-MS).
- [7] Majidnia S, Rudlin J, Nilavalan R. Investigations on a pulsed eddy current system for flaw detection using an encircling coil on a steel pipe. *Insight Non Destr Test Cond Monit.* 2014;56(10):560–565. doi: [10.1784/insi.2014.56.10.560](https://doi.org/10.1784/insi.2014.56.10.560)
- [8] Rao KSS, Rao BPC, Thirunavukkarasu S. Development of pulsed eddy current instrument and probe for detection of sub-surface flaws in thick materials. *IETE Tech Rev.* 2017;34(5):572–578. doi: [10.1080/02564602.2016.1216335](https://doi.org/10.1080/02564602.2016.1216335)
- [9] Rifai D, Abdalla A, Ali K, et al. Giant magnetoresistance sensors: a review on structures and non-destructive eddy current testing applications. *Sensors (Basel).* 2016;16(3):298. doi: [10.3390/s16030298](https://doi.org/10.3390/s16030298)
- [10] Cortés GDS, Rego D, Cavalcanti L, et al. Analysis of PEC technique and external magnetic fields for detection of corrosion under insulation: 3D finite element model. *Concilium.* 2023;23(9):483–497. doi: [10.53660/CLM-1386-23F01](https://doi.org/10.53660/CLM-1386-23F01)
- [11] Janošek M, Dressler M, Petrucha V, et al. Magnetic calibration system with interference compensation. *IEEE Trans Magn.* 2019;55(1):1–4. doi: [10.1109/TMAG.2018.2874169](https://doi.org/10.1109/TMAG.2018.2874169)
- [12] Ponikvar D, Zupanič E, Jeglič P. Magnetic interference compensation using the adaptive LMS algorithm. *Electronics.* 2023;12(11):2360. doi: [10.3390/electronics12112360](https://doi.org/10.3390/electronics12112360)
- [13] Sereda O, Korol O. The external magnetic field modeling features of electrical complexes and systems before and after its compensation. *Bull Natl Tech Univ KhPI Ser Energy Reliab Energy Effic.* 2022:79–89. doi: [10.20998/2224-0349.2022.02.01](https://doi.org/10.20998/2224-0349.2022.02.01)
- [14] Zhang Q, Wan C, Pan M, et al. A component compensation method for magnetic inter-ferential field. *J Appl Geophys.* 2017;139:331–337. doi: [10.1016/j.jappgeo.2017.01.034](https://doi.org/10.1016/j.jappgeo.2017.01.034)
- [15] Li Y, Zhao X, Liu J. Analysis of the anti-magnetic interference characteristics of the stacked magneto-optical current sensor and error compensation method. *2021 International Conference of Optical Imaging and Measurement (ICOIM) Xi'an, China*; 2021 doi:[10.1109/ICOIM52180.2021.9524430](https://doi.org/10.1109/ICOIM52180.2021.9524430).
- [16] Ferber M *et al.* Discrete optimization of EMI filter using a genetic algorithm. *2014 International Symposium on Electromagnetic Compatibility Tokyo, Japan*; 2014.
- [17] Ogirala A, Stachel JR, Mickle MH. Electromagnetic interference of cardiac rhythmic monitoring devices to radio frequency identification: analytical analysis and mitigation methodology. *IEEE Trans Inf Technol Biomed.* 2011;15(6):848–853. doi: [10.1109/TITB.2011.2163640](https://doi.org/10.1109/TITB.2011.2163640)
- [18] Gonzalez-Atienza M, Vanoost D, Verbeke M *et al.* An optimized adaptive bayesian algorithm for mitigating EMI-Induced errors in dynamic electromagnetic environments *IEEE Transactions on Electromagnetic Compatibility.* 2024 66(6): 2085-2094
- [19] Bieri O, Markl M, Scheffler K. Analysis and compensation of eddy currents in balanced SSFP. *Magn Reson Med.* 2005;54(1):129–137. doi: [10.1002/mrm.20527](https://doi.org/10.1002/mrm.20527)
- [20] Chen X, Lei Y. Electrical conductivity measurement of ferromagnetic metallic materials using pulsed eddy current method. *NDT E Int.* 2015;75:33–38. doi: [10.1016/j.ndteint.2015.06.005](https://doi.org/10.1016/j.ndteint.2015.06.005)
- [21] Desjardins D. Analytical modeling for transient probe response in eddy current testing. 2015.
- [22] Eddy I, Underhill PR, Morelli J, et al. Pulsed eddy current response to general corrosion in concrete rebar. *J Nondestr Eval Diagn Progn Eng Syst.* 2020;3(4). doi: [10.1115/1.4047851](https://doi.org/10.1115/1.4047851)
- [23] Shugg WT. *Handbook of electrical and electronic insulating materials.* New York: IEEE Press; 1995.

- [24] Ulapane N, Alempijevic A, Valls Miro J, et al. Non-destructive evaluation of ferromagnetic material thickness using pulsed eddy current sensor detector coil voltage decay rate. *NDT E Int.* 2018;100:108–114. doi: [10.1016/j.ndteint.2018.08.003](https://doi.org/10.1016/j.ndteint.2018.08.003)
- [25] Nafiah F, Tokhi MO, Majidnia S, et al. Pulsed Eddy Current: feature extraction enabling In-situ calibration and improved estimation for ferromagnetic application. *J Nondestruct Eval.* 2020;39(3). doi: [10.1007/s10921-020-00699-w](https://doi.org/10.1007/s10921-020-00699-w)